Strain engineering of the charge and spin-orbital interactions in Sr_2IrO_4

Eugenio Paris[a,1], Yi Tseng[a,2], Ekaterina M. Pärschke[b,c,2], Wenliang Zhang[a], Mary H. Upton[d], Anna Efimenko[e], Katharina Rolfs[f,g], Daniel E. McNally[a], Laura Maurel[h,i], Muntaser Naamneh[a], Marco Caputo[a], Vladimir N. Strocov[a], Zhiming Wang[j,k], Diego Casa[d], Christof W. Schneider[i], Ekaterina Pomjakushina[f], Krzysztof Wohlfeld[l], Milan Radovic[a], and Thorsten Schmitt[a,1]

[a]Photon Science Division, Paul Scherrer Institut, 5232 Villigen PSI, Switzerland; [b]Department of Physics, University of Alabama at Birmingham, Birmingham, AL 35294; [c]Institute of Science and Technology Austria, 3400 Klosterneuburg, Austria; [d]Advanced Photon Source, Argonne National Laboratory, Argonne, IL 60439; [e]European Synchrotron Radiation Facility, 38043 Grenoble, France; [f]Neutrons and Muons Research Division, Paul Scherrer Institut, 5232 Villigen PSI, Switzerland; [g]Department 8.2 Biosignals, Physikalisch-Technische Bundesanstalt Berlin, 10587 Berlin, Germany; [h]Department of Materials, Laboratory for Mesoscopic Systems, ETH Zurich, 8093 Zurich, Switzerland; [i]Laboratory for Multiscale Materials Experiments, Paul Scherrer Institute, 5232 Villigen PSI, Switzerland; [j]Key Laboratory of Magnetic Materials and Devices, Ningbo Institute of Materials Technology and Engineering, Chinese Academy of Sciences, 315201 Ningbo, China; [k]Zhejiang Province Key Laboratory of Magnetic Materials and Application Technology, Ningbo Institute of Materials Technology and Engineering, Chinese Academy of Sciences, 315201 Ningbo, China; and [l]Institute of Theoretical Physics, Faculty of Physics, University of Warsaw, PL-02093 Warsaw, Poland

Edited by Zachary Fisk, University of California, Irvine, CA, and approved August 10, 2020 (received for review June 11, 2020)

In the high spin–orbit-coupled Sr_2IrO_4, the high sensitivity of the ground state to the details of the local lattice structure shows a large potential for the manipulation of the functional properties by inducing local lattice distortions. We use epitaxial strain to modify the Ir–O bond geometry in Sr_2IrO_4 and perform momentum-dependent resonant inelastic X-ray scattering (RIXS) at the metal and at the ligand sites to unveil the response of the low-energy elementary excitations. We observe that the pseudospin-wave dispersion for tensile-strained Sr_2IrO_4 films displays large softening along the [h,0] direction, while along the [h,h] direction it shows hardening. This evolution reveals a renormalization of the magnetic interactions caused by a strain-driven cross-over from anisotropic to isotropic interactions between the magnetic moments. Moreover, we detect dispersive electron–hole pair excitations which shift to lower (higher) energies upon compressive (tensile) strain, manifesting a reduction (increase) in the size of the charge gap. This behavior shows an intimate coupling between charge excitations and lattice distortions in Sr_2IrO_4, originating from the modified hopping elements between the t_{2g} orbitals. Our work highlights the central role played by the lattice degrees of freedom in determining both the pseudospin and charge excitations of Sr_2IrO_4 and provides valuable information toward the control of the ground state of complex oxides in the presence of high spin–orbit coupling.

strain engineering | spin–orbit coupling | resonant inelastic X-ray scattering | magnetoelastic coupling | elementary excitations

In strongly correlated electron materials, the intricate entanglement of different degrees of freedom gives rise to many interesting phases and emerging phenomena such as metal–insulator transitions, colossal magnetoresistance, and superconductivity, to mention a few (1–3). The intertwined degrees of freedom, which often compete, in certain cases cooperate to establish the ground state. A prominent example for this is Sr_2IrO_4, where the large spin–orbit coupling combined with the moderate Coulomb repulsion opens a Mott-like gap in the nominally half-filled Ir *5d* t_{2g} orbitals, leading to an unexpected insulating behavior (4, 5).

Such a ground state, consisting of a single hole effectively carrying a spin-orbital total angular momentum (pseudospin) $j = 1/2$ in a square lattice, is reminiscent of the high-T_c Cu oxides. The related prediction of superconductivity (6) has fueled numerous studies in recent years, which have found impressive similarities between the two families of materials such as the presence of pseudogap (7–10), d-wave symmetry (11, 12), electron–boson coupling (13), and analogies in the magnetic excitations (14, 15). Nonetheless, superconductivity is still elusive in Sr_2IrO_4.

Since the ground-state properties are a direct consequence of the delicate balance between interwoven degrees of freedom, understanding this intricacy and finding appropriate tuning knobs promises novel functionalities. In this regard, a peculiar characteristic of Sr_2IrO_4 is the unprecedented dependence of the physical properties on the local lattice structure in the ground state (16–18). Indeed, due to the entanglement of spin and orbital degrees of freedom, the local structural details play a central role in stabilizing the canted antiferromagnetic (AF) ground state (19, 20).

Sr_2IrO_4 adopts the perovskite structure shown in Fig. 1*A*. Upon doping or temperature, the local Ir–O bond lengths change only marginally (21), while the Ir–O–Ir bond angle responds clearly (17, 22). In addition, large changes in the bond angle have been observed upon applying electrical currents (23). In all these cases, a dramatic evolution of the ground-state properties accompanies the

Significance

Understanding the relationship between entangled degrees of freedom (DOF) is a central problem in correlated materials and the possibility to influence their balance is promising toward realizing novel functionalities. In Sr_2IrO_4, the interaction between spin–orbit coupling and electron correlations induces an exotic ground state with magnetotransport properties promising for antiferromagnetic spintronics applications. Moreover, the coupling between orbital and spin DOF renders the magnetic structure sensitive to the Ir–O bond environment. To date, a detailed understanding of the microscopic spin-lattice and electron–phonon interactions is still lacking. Here, we use strain engineering to perturb the local lattice environment and, by tracking the response of the low-energy elementary excitations, we unveil the response of the microscopic spin and charge interactions.

Author contributions: M.R. and T.S. designed research; E. Paris, Y.T., E.M.P., W.Z., M.H.U., A.E., K.R., D.E.M., L.M., M.N., M.C., V.N.S., Z.W., D.C., C.W.S., E. Pomjakushina, K.W., M.R., and T.S. performed research; E. Paris and T.S. analyzed data; and E. Paris, E.M.P., K.W., and T.S. wrote the paper.

The authors declare no competing interest.

This article is a PNAS Direct Submission.

[1] To whom correspondence may be addressed. Email: eugenio.paris@psi.ch or thorsten.schmitt@psi.ch.

[2] Y.T. and E.M.P. contributed equally to this work.

This article contains supporting information online at https://www.pnas.org/lookup/suppl/doi:10.1073/pnas.2012043117/-/DCSupplemental.

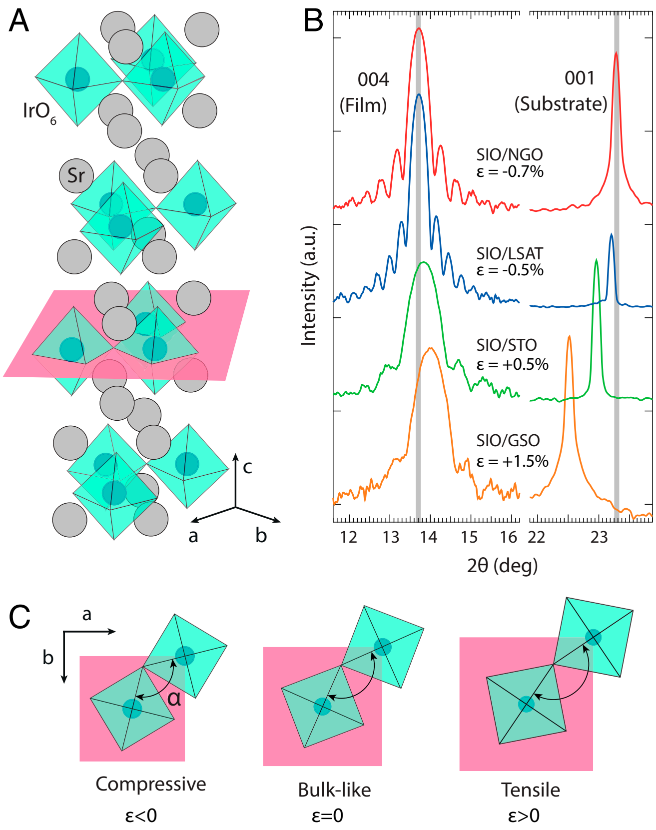

Fig. 1. Strain engineering of Sr_2IrO_4. (*A*) Crystal structure of the single-layer perovskite Sr_2IrO_4. The polyhedra represent the IrO_6 octahedron while the gray spheres represent the Sr ions. (*B*) X-ray θ-2θ diffraction scans across the (004) reflection of the Sr_2IrO_4 films grown on GSO (110), STO (100), LSAT (100), and NGO (110), showing the change in the unit cell induced by epitaxial strain. The pseudocubic (001) reflection of the substrate is also shown (on a different scale) for comparison. The data are presented on a logarithmic scale. (*C*) Pictorial view of the evolution of the local Ir–O bond in the a,b plane (cut along the plane shown in *A*) upon epitaxial strain, assuming that both the Ir–O bond length and Ir–O–Ir bond angle are evolving (not in scale). The box depicts the relative expansion/compression of the pseudocubic unit cell.

change in the lattice structure. Such findings leave open the question on the role of the lattice, separated from other contributions such as band filling or disorder, urging for an approach involving direct manipulation of the bond geometry. Efforts in this direction provided promising results in view of controlling the ground-state properties. For instance, the application of hydrostatic pressure quenches the local magnetic moment of Sr_2IrO_4 (24) and induces a magnetic cross-over, characterized by the renormalization of the exchange couplings (25). Besides external pressure, epitaxial strain—achieved by growing thin films of Sr_2IrO_4 on substrates with mismatching in-plane lattice parameter—allows exerting very high biaxial pressure along the Ir–O bond network in the basal plane (26, 27), as shown schematically in Fig. 1*C*. Epitaxial strain can also affect the Ir–O–Ir bond angle, on which the hierarchy between isotropic and anisotropic pseudospin interactions is expected to depend (16). In previous reports, a decrease in the zone-boundary magnon (28) and bimagnon (29) energy was found upon tensile strain, accompanied by an increased Néel temperature (28). Moreover, theoretical proposals suggest the Mott gap to shrink upon compressive strain, driving the system toward an insulator-to-metal transition (30).

Due to its giant anisotropic magnetoresistance, Sr_2IrO_4 is a promising material in the novel field of AF spintronics (31–33). For such applications, it is pivotal to be able to control the magnetic interactions via strain in few-nanometer thin films in the prospect of integrating such material layers into actual devices. In this regard, it is important to obtain information on the evolution of microscopic electronic quantities and the related low-energy elementary excitations in response to the lattice tuning. Such information is also highly valuable toward a better understanding of the magnetoelastic coupling (16, 18, 23, 34, 35) and electron–phonon coupling (13, 36, 37) in Sr_2IrO_4.

In this work, we investigate the strain effects on the spin-orbital and charge excitations of Sr_2IrO_4 using a combination of O K-edge and Ir L_3-edge resonant inelastic X-ray scattering (RIXS). We find the local bond geometry to control the nature of the pseudospin exchange, effectively modulating the degree of anisotropy of the magnetic interactions. The modification of the magnetic dispersion is accompanied by a continuous evolution of the low-energy electronic structure, revealed by a large change in the electron–hole pair excitations. In particular, the strain-induced enhancement of the electron hopping strength causes a renormalization in the size of the Mott gap.

Results and Discussion

In recent years, intense efforts have been made to exploit the electron–lattice coupling to induce new functionality in Sr_2IrO_4. An important missing piece of knowledge in this regard is the study of the collective elementary excitations upon tuning the lattice parameters, which can only be probed using advanced spectroscopies such as RIXS. So far, Ir L_3-edge RIXS has been extensively employed to study iridium oxide materials in the bulk form (14, 15, 38–47). It was recently reported that, due to the large metal–ligand hybridization combined with high spin–orbit coupling at the metal ion, information on the elementary excitations can be extracted using an indirect RIXS process at the O K edge (48). One of the advantages of this approach is the lower penetration depth of soft X-rays, providing high sensitivity to ultrathin samples such as films.

Fig. 2 *C* and *D* display the Ir L_3-edge and O K-edge RIXS spectra, respectively, both measured at the in-plane momentum transfer $\boldsymbol{Q} = (1/4, 0)$ reciprocal lattice units (r.l.u.) on a Sr_2IrO_4 thin film with $\varepsilon = -0.5\%$ compressive strain. In the O K-edge RIXS experiment, we tune the incoming photon energy to a particular absorption peak, allowing isolation of the contribution to the RIXS signal from the planar oxygen $2p_x/2p_y$ orbitals, hybridized with the Ir 5*d* orbitals (*SI Appendix*, Fig. S3*B*). In the Ir L_3-edge RIXS experiment, instead, the incoming photon energy is tuned to the L_3 X-ray absorption resonance, corresponding to the Ir $2p_{3/2}$-$5d$ transition and being directly sensitive to the elementary excitations involving the Ir *d* shell. Both the Ir L_3 and O K-edge RIXS spectra show single $j = 1/2$ pseudospin-flip excitations centered around 150-meV energy loss (labeled "M" in Fig. 2). The high sensitivity to spin excitations is due to the presence of strong spin–orbit coupling in the intermediate state in the former case (49) and sizable spin–orbit coupling in the valence band in the latter (48). The magnetic excitations are more intense in the L_3-edge spectrum while broader and less defined in the O K-edge spectrum due to the presence of a large bi (multi)-magnon tail. Both spectra show an intense structure from 0.5 to 1-eV energy loss due to orbital excitations between $j = 3/2$ and $j = 1/2$ manifolds (14, 42). On the other hand, the main qualitative difference between the Ir L_3-edge and O K-edge RIXS spectrum is the higher sensitivity of the latter to an excitation located at ~400-meV energy loss (labeled "A" in Fig. 2). As we will discuss later, this excitation is sensitive to the carrier dynamics through electron–hole pair excitations.

Before discussing the evolution of the elementary excitations probed by RIXS, we briefly discuss the possible effects of epitaxial strain on the local structure of Sr_2IrO_4. The x-ray diffraction scans in Fig. 1B show a continuous change in the unit

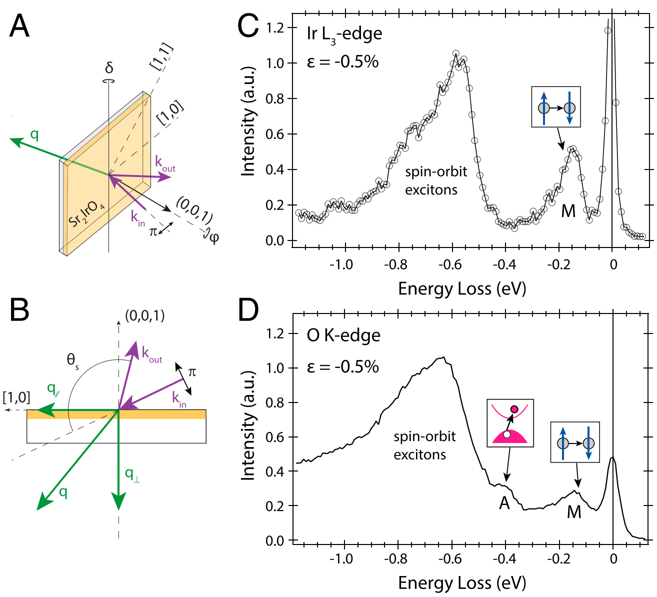

Fig. 2. Ir L_3- and O K-edge RIXS experiments. (*A* and *B*) Sketch of the experimental geometry for the RIXS experiment. The scattering angle θ_S is set to 130° for the O K-edge measurements and 90° for the Ir L_3-edge measurements. (*C*) Ir L_3-edge RIXS spectrum on a thin film of Sr_2IrO_4 grown on LSAT (100) with a $\varepsilon = -0.5\%$ compressive strain, measured near $\boldsymbol{Q} = (0.25, 0)$. (*D*) O K-edge RIXS spectrum on the same sample, taken at π-polarization and $\boldsymbol{Q} \sim (0.25, 0)$. The pseudospin-flip mode is labeled "M" while the electron-hole pairs excitations are labeled "A." The intense spin–orbit exciton structure (j = 3/2 to j = 1/2 excitation) is also indicated. (*Insets*) A pictorial view of the electron–hole (peak A) and pseudospin-flip (peak M) excitations.

cell caused by the strain. In perovskite oxide materials, the epitaxial strain is expected to induce rotations of the metal-oxide octahedra (Fig. 1*C*). Namely, tensile (compressive) strain tends to increase (decrease) the Ir–O–Ir bond angle (26, 27). However, to what extent this rotation would be "rigid" in Sr_2IrO_4 is not clear, as a concomitant modulation of the Ir–O bond length is likely at play (28, 30, 50).

In the following, we will first address the effect of strain on the isospin excitations and then discuss the evolution of the low-energy band structure by analyzing the electron–hole pair excitations. The orbital excitations are also modified by strain; a brief discussion on this aspect can be found in *SI Appendix*.

Tuning the Magnetic Interactions. The momentum dependence of the Ir L_3-edge RIXS spectrum for a Sr_2IrO_4 thin film with $\varepsilon = -0.5\%$ compressive strain is presented in Fig. 3*A*. In this sample, as well as in all others investigated in this study, the collective magnetic excitation disperses away from the AF zone center and reaches the band top at the AF zone boundaries, in good agreement with reports on single crystals of Sr_2IrO_4 (14, 38, 40, 46). In Fig. 3 *B* and *C*, we present the evolution of the magnetic excitation as a function of strain at the zone boundaries (1/2, 0) and (1/4, 1/4), respectively. The magnetic excitation shifts to lower energies upon tensile strain at $\boldsymbol{Q} = (1/2, 0)$, while an opposite behavior is observed at $\boldsymbol{Q} = (1/4, 1/4)$, where the magnetic mode hardens. An anisotropic response of the magnetic excitations is reminiscent of electron doping, affecting mainly the [h,h] direction in La-doped Sr_2IrO_4 (38, 40, 46) and $Sr_3Ir_2O_7$ (45, 47). It is worth noting that the present anisotropic evolution is dissimilar to the case of a Mott insulator such as La_2CuO_4, in which epitaxial strain affects the magnetic dispersion in a similar way along the nodal and antinodal directions (51). As summarized in Fig. 3*D*, upon expanding the lattice structure to $\varepsilon = 1.5\%$, the magnetic modes along the [h,0] and [h,h] directions of the AF zone tend to reach a similar energy scale. In order to fully probe the reciprocal lattice, we combine RIXS measurements at the O K- and Ir L_3 edge to uncover the full dispersion of the magnetic excitations. For each sample, we performed at least one measurement at both O K- and Ir L_3 edge at a given $\boldsymbol{Q}$ vector, to ensure the compatibility between the dispersion obtained from the two datasets. The different components in the RIXS spectra are fitted using multiple peak functions. A typical fit obtained for O K-edge and Ir L_3 edge at the same exchanged wave vector on a Sr_2IrO_4/LSAT film ($\varepsilon = -0.5\%$) is presented in Fig. 4*E*. The magnetic dispersion, obtained for different strain levels, is presented in Fig. 4 *A*–*D*. When the strain level is small ($\varepsilon = \pm 0.5\%$), the spin-wave dispersion resembles the one observed in the single crystal (14, 40), reaching a band top of ~200 meV at $\boldsymbol{Q} = (1/2, 0)$ and ~100 meV at $\boldsymbol{Q} = (1/4, 1/4)$. For higher compressive strain ($\varepsilon = -0.7\%$) the dispersion shows a reduced curvature along the [h,0] direction and tends to reach higher energy at the zone boundary. Upon large tensile strain ($\varepsilon = +1.5\%$) the dispersion presents an increased curvature and a large softening at $\boldsymbol{Q} = (1/2, 0)$, with a band top of ~160 meV. The softening is accompanied by a hardening at $\boldsymbol{Q} = (1/4, 1/4)$, where the magnetic mode reaches ~130 meV.

In order to capture the evolution of the exchange couplings upon strain, we fit the spin-wave dispersion using the anisotropic Heisenberg model with longer-range spin interactions, which was

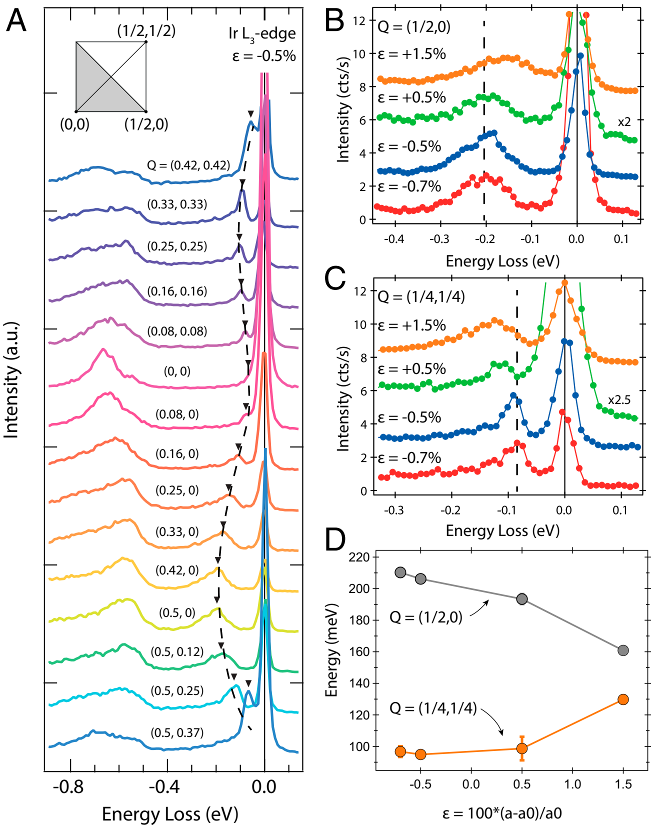

Fig. 3. Strain and momentum-dependent Ir L_3-edge RIXS. (*A*) Ir L_3-edge RIXS spectra recorded on a thin film of Sr_2IrO_4 grown on LSAT(100), with $\varepsilon = -0.5\%$ compressive strain for different exchanged momenta (as labeled). (*Inset*) The reciprocal unit cell and the AF magnetic zone (gray area). (*B* and *C*) Low-energy region of the Ir L_3-edge RIXS spectra at $\boldsymbol{Q} = (1/2, 0)$ and $\boldsymbol{Q} = (1/4, 1/4)$. Data from films grown on different substrates are shown with a vertical offset. The data for $\varepsilon = +0.5\%$ are multiplied by a constant for better visualization (see label). The vertical dashed line is a guide to the eye. (*D*) Energy of the collective magnetic excitation at the (1/2, 0) and (1/4, 1/4) zone boundaries as a function of strain.

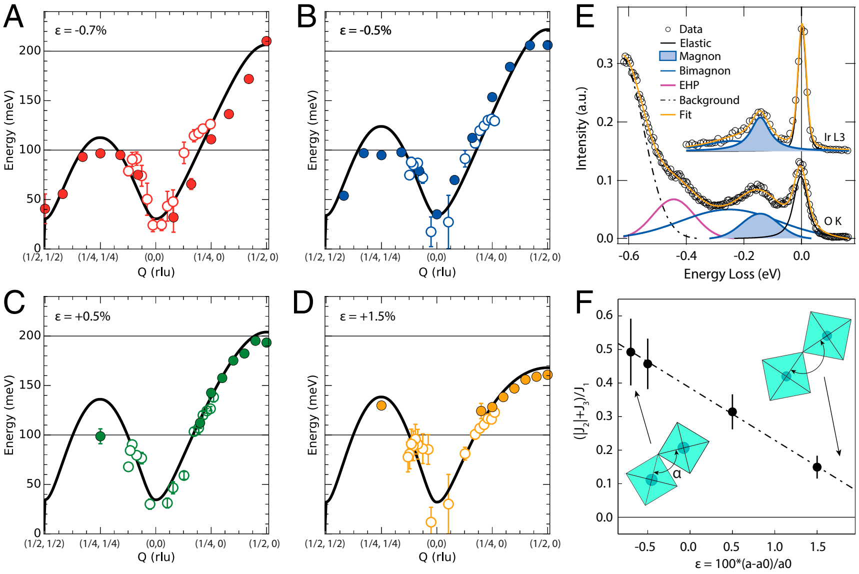

Fig. 4. Tuning of the spin-wave mode by epitaxial strain. (*A*–*D*) Dispersion of the collective magnetic excitations in Sr_2IrO_4 as a function of the epitaxial strain. The data are obtained from combining the O K-edge (empty symbols) and Ir L_3-edge RIXS spectra (full symbols). The black solid line is a fit to an anisotropic Heisenberg model (see text). (*E*) Comparison between the fitting model used for O K-edge (*Lower*) and Ir L_3-edge (*Upper*) spectra at $\boldsymbol{Q}$ = (0.25, 0) for ε = −0.5%. The data (black circles) are presented along with the best fit (orange solid line). The different fitting components are shown (see label). (*F*) Strain dependence of the ratio between the magnitude of the higher-order exchange interactions ($|J_2|+J_3$) and the first-nearest-neighbor exchange interaction (J_1). (*Insets*) A pictorial view of the evolution of the Ir–O–Ir bond upon strain.

recently used to model the magnetic excitations in a bulk Sr_2IrO_4 crystal (38, 52) (*SI Appendix*, Eq. **S3**). The best fit, obtained for different strain levels, is shown as a solid black line in Fig. 4 *A*–*D* and the obtained exchange couplings are reported in Table 1. By increasing the tensile strain, the first- (J_1), second- (J_2), and third-nearest-neighbor (J_3) exchange-coupling parameters clearly evolve. The relatively large decrease of the longer-range spin exchanges (J_2 and J_3) upon increase of the tensile strain is consistent with an associated decrease of the hopping parameters, as pointed out in recent Raman investigations (29). On the other hand, the nearest-neighbor spin exchange J_1 experiences relatively small but nonmonotonic changes with the increase of the tensile strain. Fig. 4*F* shows the dependence on strain of the ratio of the second- and third-neighbor exchange interactions with respect to the first (nearest) neighbor exchange ($(|J_2|+J_3)/J_1$). When ε = −0.7%, the longer-range spin interactions reach up to 50% of the nearest-neighbor exchange. By applying tensile strain, this ratio decreases linearly and, when ε = +1.5%, the spin interactions evolve toward a nearest-neighbor Heisenberg-like behavior, with longer-range correlations accounting only for ~15% of J_1. In this regard, tensile strain makes the isospin-wave dispersion similar to the spin-wave dispersion observed in cuprates. For comparison, in correlated cuprate insulators such as La_2CuO_4, the importance of longer-range terms is ~10% (53).

It has been proposed that a Mott insulator, with strong on-site spin–orbit coupling and metal–oxygen–metal bond close to 180°, can be described with a magnetic Hamiltonian composed of Heisenberg-like interactions with a dominant nearest-neighbor exchange (J_1). Such a model contains only small anisotropic corrections, and the magnetic dispersion is expected to be similar along the [h,0] and [h,h] directions of the reciprocal lattice. In Sr_2IrO_4 however, the presence of octahedral rotations enhances the importance of Dzyaloshinskii–Moriya and other anisotropic interactions (16). The resulting magnetic dispersion of Sr_2IrO_4 shows a different behavior along the [h,0] and [h,h] directions, requiring inclusion of sizable second- and third-nearest-neighbor exchange interactions (J_2 and J_3) in the model calculations. Moreover, in most 3*d* Mott insulators, the AF order arises among localized S = 1/2 spins, naturally allowing mapping the spin interactions into a Heisenberg model with local interactions. In Sr_2IrO_4 on the other hand, the delocalized nature of the 5*d* orbitals suggests describing the ground state in an intermediate Mott–Slater regime, i.e., to assume a moderate value of the Coulomb repulsion (as compared to the kinetic energy of the electrons) (54). Importantly, the values of J_2 and J_3 obtained experimentally for bulk single crystals of Sr_2IrO_4 are as large as 33% and 25% of J_1 in magnitude, respectively. The nonlocal interactions are thus implicitly included in the phenomenological model through the large higher-order exchange terms. Crucially, the J_1-J_2-J_3 Heisenberg model with longer-range spin interactions employed here describes remarkably well the observed experimental pseudospin-wave dispersion (14, 38, 40) which justifies its choice in this work.

Tuning the Low-Energy Electronic Structure. In the following, we address the nature of peak A in the O K-edge RIXS spectrum. Through this mode, we can track the evolution of the low-energy electronic structure of Sr_2IrO_4 upon misfit strain. Fig. 5*A* shows the O K-edge RIXS spectra of a thin film of Sr_2IrO_4 with ε = −0.5%, measured by varying the exchanged momentum in the reciprocal space. Peak A appears as a dispersive mode with a minimum located at the zone center. This excitation has been observed in various iridate compounds (40, 42, 55) but its nature is not well understood. The energy scale (300–400 meV) is of the

Table 1. Values of the exchange parameters obtained from the least-square fit of the experimental spin-wave dispersion in strained Sr_2IrO_4 films

Substrate (ε)	J_1, meV	J_2, meV	J_3, meV
NGO (−0.7%)	65.0 (±8.0)	−17 (±4.5)	15 (±2.0)
LSAT (−0.5%)	72.2 (±7.0)	−17 (±3.9)	16 (±1.6)
STO (+0.5%)	73.2 (±5.4)	−12 (±2.9)	11 (±1.7)
GSO (+1.5%)	68.3 (±3.6)	−5.6 (±1.9)	4.6 (±1.1)

For the model fit function, see *SI Appendix*, Eq. S3.

order of magnitude of the on-site Coulomb interaction and similar to the optical gap energy (26, 36, 56), suggesting that this excitation is related to the formation of electron–hole pairs. Indeed, this excitation is reported to be in the same energy range also in Na_2IrO_3 (55), having a band gap similar to Sr_2IrO_4 and absent (in this energy range) in $Sr_3Ir_2O_7$ having a smaller charge gap (48). Theoretical work suggested it results from the interaction between optical electron–hole excitations and the spin–orbit exciton modes (57). Moreover, previous RIXS reports ascribed it to an additional branch of the spin–orbit exciton (40), possibly involving a Jahn–Teller-like distortion in the t_{2g} orbitals (58).

To clarify the origin of this excitation, we compute the RIXS intensity for an electron–hole interband transition by evaluating the momentum-resolved joint density of states $N(\omega,\boldsymbol{Q})$, using the following equation (59):

$$N(\omega,\boldsymbol{Q}) = \sum_{\nu} \int_{V} d\boldsymbol{k} \int_{V'} d\boldsymbol{k}'\, \delta(\hbar\omega - \epsilon_\nu(\boldsymbol{k}) - \epsilon_c(\boldsymbol{k}'))\delta(\boldsymbol{k} - \boldsymbol{k}' - \boldsymbol{Q}), \quad [1]$$

where ϵ_ν and ϵ_c represent the valence (occupied) and conduction (unoccupied) bands involved in the electron–hole pair formation. In our notation, ω is the energy lost by the photon in the RIXS process and $\boldsymbol{Q}$ is the exchanged momentum. Since this calculation requires the knowledge of $\epsilon_\nu(\boldsymbol{k})$ and $\epsilon_c(\boldsymbol{k})$ across the whole reciprocal space, we calculate the dispersions of the electron removal and addition states using single-particle Green functions, accounting for electron–electron correlations in a nonperturbative way, as was recently used to describe photoemission and inverse photoemission spectral functions, respectively (60) (see *SI Appendix* for details). Finally, we account for the experimental resolution adding a finite Gaussian broadening to the obtained spectrum. The resulting momentum and energy-dependent spectral function for the low-energy electron–hole pair excitations (EHP) in Sr_2IrO_4 is presented in Fig. 5*B*. In our calculation, when the energy loss equals the indirect charge gap at ∼250 meV (7), we observe a continuum in the $N(\omega,\boldsymbol{Q})$ due to the onset of electron–hole transitions. On top of such a broad structure, we identify a dispersive mode featuring a U-shaped dispersion, with a bottom located at $\boldsymbol{Q} = (0,0)$. Our calculation captures well the overall behavior of peak A, allowing us to assign it to an interband EHP. The value of the energy minimum at the zone center provides information on the optical gap, for which experimental reports range from ∼300 meV (26, 36) to 550 meV (56). It is worth noting that the onset of the EHP overlaps with the many-body magnetic excitations, located between 200 and 300 meV, indicating a possible interaction between charge and isospin degrees of freedom.

To address the effect of strain on the electronic structure of Sr_2IrO_4, we collect momentum-dependent O K-edge RIXS on our series of strained thin films. Fig. 5*C* shows the strain dependence of peak A, measured near $\boldsymbol{Q} = (0,0)$. As one can see, the strain directly affects the energy of this mode, suggesting the underlying modification of the low-energy electronic structure. In particular, peak A hardens in energy upon tensile strain. We analyzed the dependence of the excitation energy on strain and momentum by a detailed peak fitting (see, for example, Fig. 4*E*). The momentum dispersion of peak A upon various strain values

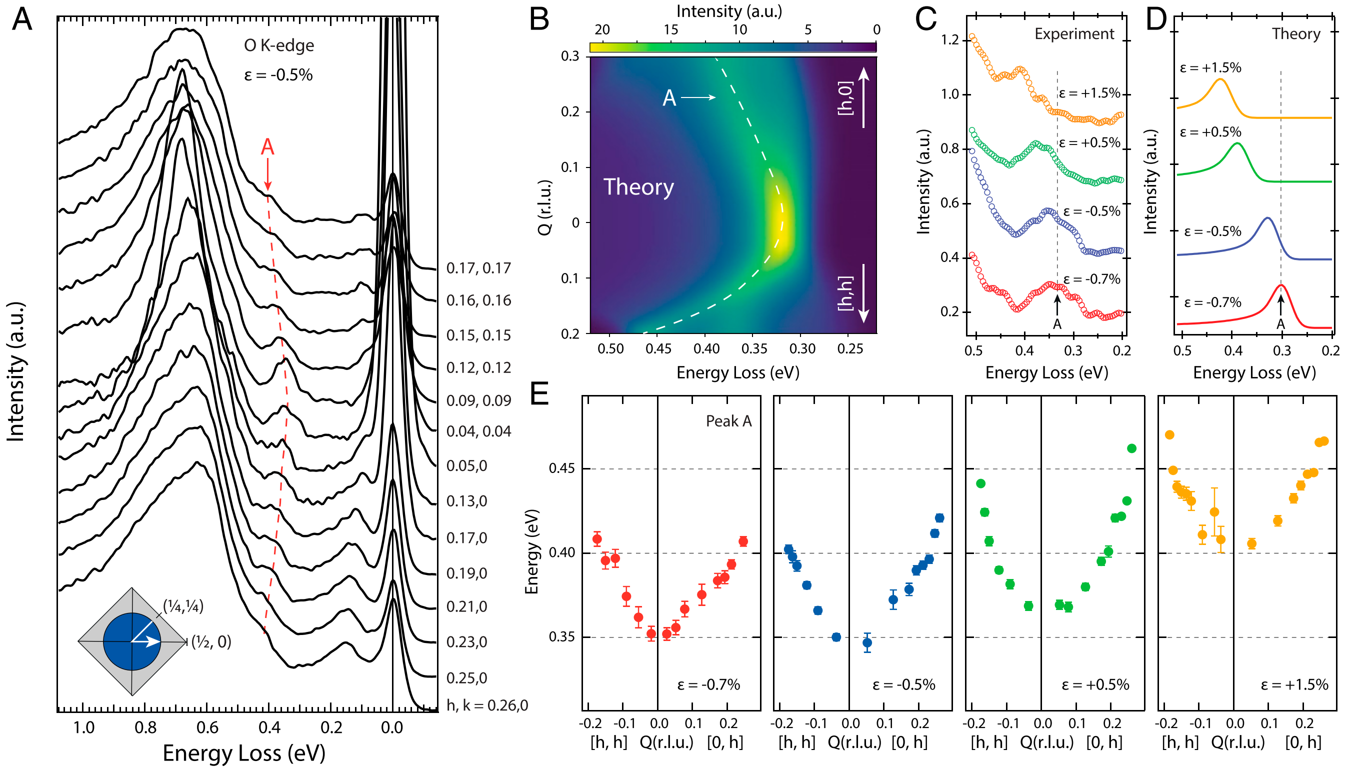

Fig. 5. Electron-hole pair (EHP) excitations from O K-edge RIXS. (*A*) Momentum dependence of the O K-edge RIXS spectrum of a thin film of Sr_2IrO_4 under $\varepsilon = -0.5\%$ compressive strain, taken at 20 K with π-polarized light. (*Inset*) Representation of the path followed in the reciprocal space (white arrow). The gray square represents the magnetic zone of Sr_2IrO_4 while the blue sphere shows the maximum probing volume accessible at the O K edge. The red dashed line marks the position of peak A. (*B*) Colormap representing the theoretical RIXS intensity for the EHP excitation as a function of the exchanged energy and momentum, calculated as discussed in the main text. (*C*) The EHP excitation from O K-edge RIXS for different strain levels, taken at $\boldsymbol{Q} \sim (0.04,0)$ r.l.u. (*D*) Calculated O K-edge RIXS intensity for an EHP excitation at $\boldsymbol{Q} = (0.04,0)$ as a function of strain (see main text for details). The vertical dashed line is a guide to the eye, marking the position of peak A for the highest compressive strain. (*E*) Energy dispersion of the EHP excitations (peak A) obtained by fitting the O K-edge RIXS spectra. Different panels represent different strain levels.

is shown in Fig. 5*E*. Regardless of the strain level, this excitation shows a gap at the zone center and disperses, rather symmetrically, along the [h,0] and [h,h] directions. The strain appears to modulate the electron–hole bandwidth, and a large increase in the size of the gap at $\boldsymbol{Q} = (0,0)$ is observed upon tensile strain. We note that the hardening of peak A resembles the evolution of the "α-peak" observed in optical spectroscopy that was associated with a reduction of the U/t ratio (26, 61). In particular, Nichols et al. (26) found the optical gap to increase (decrease) upon tensile (compressive) strain. The present findings are in agreement with this scenario and suggest that the material is evolving toward a metallic state upon compressive strain. We observe that going from a compressive strain of −0.7% to a tensile strain of +1.5% we detect a change in the direct charge gap of about ∼60 meV. For comparison, upon hydrostatic pressure as large as 30 GPa, the change in the insulating gap inferred from transport measurements was ∼30 meV (24). This finding shows the effectiveness of epitaxial strain in tuning the electronic structure by distorting the local Ir-O environment. Nonetheless, the gap remains sizable as a function of strain, allowing us to employ the same approach, based on the localized limit, to describe the charge and spin excitations.

In order to understand the evolution of the EHP excitations microscopically, we compute the joint density of states $N(\omega,\boldsymbol{Q})$ for different strain levels using Eq. (**1**). To account for the strain effects, we firstly assume an exponential scaling of the orbital-dependent hopping parameters as a function of the in-plane lattice constant, as in ref. 62. Secondly, we adapt the exchange-coupling parameters to those obtained from fitting the experimental magnetic dispersion for various strain levels, as shown in Fig. 4 *A*–*D* (details in *SI Appendix*). The result of this calculation is shown in Fig. 5*D* at the same momentum transfer vector $\boldsymbol{Q}$ as the data in Fig. 5*C*. The model captures well the evolution of the excitation gap upon strain, i.e., the charge gap increases with increasing ε. In this material, the size of the Mott gap depends not only on the on-site Coulomb repulsion U, but also on the binding energies of the so-called magnetic polarons, which are composed of charge carriers coupled to the magnetic $J = 1/2$ excitations (*SI Appendix*). Since U is a local interaction, we assume that this would change only negligibly in the considered range of strain. Therefore, we ascribe the observed increase of the charge gap upon tensile strain to a decrease in the binding energy of magnetic polarons in both valence and conduction bands. Such binding energy depends on the ratios of the spin-exchange parameters J with respect to the hopping parameters t (63). In particular, the exchange parameters J_2 and J_3 are responsible for the free hopping of the magnetic polaron and contribute mostly to its bandwidth. Upon tensile strain, J_2 and J_3 decrease quicker than the coupling of the holes and electrons to the magnetic background (∼t) (63), causing the decrease of polaron binding energies resulting in the effective tuning of the charge gap.

As discussed earlier, a reduction of the lattice parameter corresponds locally to a reduction of the Ir–O bond length and/or an enhanced rotation of the IrO_6 octahedra. While a rise in the hopping parameters follows naturally a decrease in the Ir–O bond length, such a development is not obvious for an increase in the octahedral rotation. Indeed, it apparently contradicts the existing paradigm in transition-metal oxides, that the closer the metal–oxygen–metal angle is to 180°, the more effective is the hopping mechanism. However, such a picture assumes that the spin–orbit coupling is small enough to separate the single-particle wave functions into their spin and orbital sectors. In 5d oxides, such separation is no longer valid and the evolution of the hopping integrals as a function of the bond angle becomes more complicated. In this regard, recent work pointed toward a net increase in the overall hopping integral t between the $J_{\mathrm{eff}} = 1/2$ electrons upon compressive strain (29).

Finally, it is worth noticing that in this material the low-energy electronic structure is largely temperature-dependent (36). Since our results are obtained at a fixed temperature of 20 K, exploring the effect of strain in the elementary excitations as a function of temperature would represent an interesting outlook for future experiments.

Conclusions

We have used RIXS to resolve the effect of the epitaxial strain on the elementary excitations of Sr_2IrO_4. In particular, we have identified EHP excitations, mapped their momentum dependence, and found that the epitaxial strain alters the energy scale of such excitations, indicating a substantial increase in the size of the Mott gap upon tensile strain. With the aid of state-of-the-art model calculations, we show that such an evolution of the Mott gap follows the ratio of the spin exchange with respect to the hopping integral, which is responsible for the coupling between electrons (and holes) to the spin excitations in the AF background. In particular, under tensile strain, the collective magnetic excitations undergo a large softening at the magnetic zone boundary $\boldsymbol{Q} = (1/2, 0)$, accompanied by hardening at $\boldsymbol{Q} = (1/4, 1/4)$. This behavior entails an evolution from long-range anisotropic toward nearest-neighbor Heisenberg-like pseudospin interactions upon tensile strain. We suggest that the change in the Ir–O–Ir bond angle, induced by the strain, is responsible for the change in the degree of anisotropy in the magnetic interactions. However, the observed cross-over from short-range to long-range interactions may also originate in a transition from Mott-like to Slater-like physics. Altogether, this suggests that the localized limit might be more appropriate to describe the system in the tensile-strain case, where the effective magnetic interactions are more akin to the "high-T_c" copper oxides. Conversely, the importance of nonlocal interactions seems to increase upon compressive strain. Indeed, such a scenario is also corroborated by the changes in the size of the charge gap, being larger upon tensile strain. In summary, our study provides a microscopic view of the electron- and pseudospin–lattice interaction in Sr_2IrO_4 and demonstrates that epitaxial strain, combined with other tuning knobs such as doping or interface engineering, is a promising route toward inducing new functional properties in high spin–orbit-coupled oxides.

Materials and Methods

Thin films of Sr_2IrO_4 were grown on $GdScO_3(110)$ (GSO), $SrTiO_3(100)$ (STO), $(LaAlO_3)_{0.3}(Sr_2AlTaO_6)_{0.7}(100)$ (LSAT), and $NdGaO_3(110)$ (NGO) by pulsed laser deposition to achieve an in-plane strain ε = +1.5%, +0.5% and −0.5% and −0.7%, respectively. In our convention, $\varepsilon = 100*(a-a_0)/a_0$ where a and a_0 are the strained and bulk pseudocubic in-plane lattice parameters. The epitaxial strain levels are experimentally determined using X-ray diffraction. The X-ray absorption and RIXS measurements at the O K edge (∼530 eV) were carried out at the ADRESS beamline of the Swiss Light Source, Paul Scherrer Institut (64). The Ir L_3-edge (∼11.214-KeV) RIXS measurements were performed at the ID20 beamline of the European Synchrotron Radiation Facility (ESRF) (65) and at the 27 ID-B beamline of the Advanced Photon Source (APS) (66). The sample temperature was kept at 20 K during all measurements. The magnetic dispersion, measured with RIXS, was fitted with an anisotropic Heisenberg model with first-, second-, and third-neighbor contributions (*SI Appendix*, Eq. **S3**) (38, 52), and the exchange parameters for each sample were obtained employing least-square fitting. Theoretical predictions of the intensity and dispersion of the EHP excitations measured in O K-edge RIXS were obtained by numerically integrating the occupied and unoccupied bands over momentum space. The dispersion of valence (conduction) bands was obtained using an extended multiplet *t-J*-like model evaluated using Green functions in the framework of the self-consistent Born approximation (60, 67). Details of the sample preparation, experimental conditions, and calculation methods can be found in *SI Appendix*.

Data Availability. All study data are included in the article and *SI Appendix* and can be obtained from the corresponding authors upon reasonable request.

ACKNOWLEDGMENTS. We gratefully acknowledge C. Sahle for experimental support at the ID20 beamline of the ESRF. The soft X-ray experiments were carried out at the ADRESS beamline of the Swiss Light Source, Paul Scherrer Institut (PSI). E. Paris and T.S. thank X. Lu and C. Monney for valuable discussions. The work at PSI is supported by the Swiss National Science Foundation (SNSF) through Project 200021_178867, the NCCR (National Centre of Competence in Research) MARVEL (Materials' Revolution: Computational Design and Discovery of Novel Materials) and the Sinergia network Mott Physics Beyond the Heisenberg Model (MPBH) (SNSF Research Grants CRSII2_160765/1 and CRSII2_141962). K.W. acknowledges support by the Narodowe Centrum Nauki Projects 2016/22/E/ST3/00560 and 2016/23/B/ST3/00839. E.M.P. and M.N. acknowledge funding from the European Union's Horizon 2020 research and innovation programme under the Marie Sklodowska-Curie Grant Agreements 754411 and 701647, respectively. M.R. was supported by the Swiss National Science Foundation under Project 200021 – 182695. This research used resources of the APS, a U.S. Department of Energy (DOE) Office of Science User Facility operated for the DOE Office of Science by Argonne National Laboratory under Contract DE-AC02-06CH11357.

1. Y. Tokura, M. Kawasaki, N. Nagaosa, Emergent functions of quantum materials. *Nat. Phys.* **13**, 1056–1068 (2017).
2. D. I. Khomskii, *Transition Metal Compounds*, (Cambridge University Press, 2014).
3. M. Imada, A. Fujimori, Y. Tokura, Metal-insulator transitions. *Rev. Mod. Phys.* **70**, 1039–1263 (1998).
4. B. J. Kim *et al.*, Novel J_{eff}=1/2 Mott state induced by relativistic spin-orbit coupling in Sr_2IrO_4. *Phys. Rev. Lett.* **101**, 076402 (2008).
5. G. Cao, J. Bolivar, S. McCall, J. Crow, R. Guertin, Weak ferromagnetism, metal-to-nonmetal transition, and negative differential resistivity in single-crystal Sr_2IrO_4. *Phys. Rev. B* **57**, R11039–R11042 (1998).
6. F. Wang, T. Senthil, Twisted Hubbard model for Sr_2IrO_4: Magnetism and possible high temperature superconductivity. *Phys. Rev. Lett.* **106**, 136402 (2011).
7. A. de la Torre *et al.*, Collapse of the Mott gap and emergence of a nodal liquid in lightly doped Sr_2IrO_4. *Phys. Rev. Lett.* **115**, 176402 (2015).
8. Y. J. Yan *et al.*, Electron-doped Sr_2IrO_4: An analogue of hole-doped cuprate superconductors demonstrated by scanning tunneling microscopy. *Phys. Rev. X* **5**, 041018 (2015).
9. I. Battisti *et al.*, Universality of pseudogap and emergent order in lightly doped Mott insulators. *Nat. Phys.* **13**, 21–25 (2017).
10. Y. K. Kim *et al.*, Superconductivity. Fermi arcs in a doped pseudospin-1/2 Heisenberg antiferromagnet. *Science* **345**, 187–190 (2014).
11. Y. K. Kim, N. H. Sung, J. D. Denlinger, B. J. Kim, Observation of a d-wave gap in electron-doped Sr_2IrO_4. *Nat. Phys.* **12**, 37–41 (2016).
12. K. Terashima *et al.*, Evolution of the remnant Fermi-surface state in the lightly doped correlated spin-orbit insulator $Sr_{2-x}La_xIrO_4$. *Phys. Rev. B* **96**, 041106(R) (2017).
13. Y. Hu *et al.*, Spectroscopic evidence for electron-boson coupling in electron-doped Sr_2IrO_4. *Phys. Rev. Lett.* **123**, 216402 (2019).
14. J. Kim *et al.*, Magnetic excitation spectra of Sr_2IrO_4 probed by resonant inelastic x-ray scattering: Establishing links to cuprate superconductors. *Phys. Rev. Lett.* **108**, 177003 (2012).
15. J. P. Clancy *et al.*, Magnetic excitations in hole-doped Sr_2IrO_4: Comparison with electron-doped cuprates. *Phys. Rev. B* **100**, 104414 (2019).
16. G. Jackeli, G. Khaliullin, Mott insulators in the strong spin-orbit coupling limit: From Heisenberg to a quantum compass and Kitaev models. *Phys. Rev. Lett.* **102**, 017205 (2009).
17. M. Ge *et al.*, Lattice-driven magnetoresistivity and metal-insulator transition in single-layered iridates. *Phys. Rev. B* **84**, 100402 (2011).
18. H. Liu, G. Khaliullin, Pseudo-Jahn-Teller effect and magnetoelastic coupling in spin-orbit Mott insulators. *Phys. Rev. Lett.* **122**, 057203 (2019).
19. M. K. Crawford *et al.*, Structural and magnetic studies of Sr_2IrO_4. *Phys. Rev. B* **49**, 9198–9201 (1994).
20. S. Boseggia *et al.*, Locking of iridium magnetic moments to the correlated rotation of oxygen octahedra in Sr_2IrO_4 revealed by x-ray resonant scattering. *J. Phys. Condens. Matter* **25**, 422202 (2013).
21. K. Terashima *et al.*, Determination of the local structure of $Sr_{2-x}M_xIrO_4$ (M = K, La) as a function of doping and temperature. *Phys. Chem. Chem. Phys.* **20**, 23783–23788 (2018).
22. Q. Huang *et al.*, Neutron powder diffraction study of the crystal structures of Sr_2RuO_4 and Sr_2IrO_4 at room temperature and at 10 K. *J. Solid State Chem.* **112**, 355–361 (1994).
23. G. Cao *et al.*, Electrical control of structural and physical properties via strong spin-orbit interactions in Sr_2IrO_4. *Phys. Rev. Lett.* **120**, 17201 (2018).
24. D. Haskel *et al.*, Pressure tuning of the spin-orbit coupled ground state in Sr_2IrO_4. *Phys. Rev. Lett.* **109**, 027204 (2012).
25. D. Haskel *et al.*, Possible quantum paramagnetism in compressed Sr_2IrO_4. *Phys. Rev. Lett.* **124**, 067201 (2020).
26. J. Nichols *et al.*, Tuning electronic structure via epitaxial strain in Sr_2IrO_4 thin films. *Appl. Phys. Lett.* **102**, 141908 (2013).
27. L. Miao, H. Xu, Z. Q. Mao, Epitaxial strain effect on the J_{eff} = 1/2 moment orientation in Sr_2IrO_4 thin films. *Phys. Rev. B* **89**, 035109 (2014).
28. A. Lupascu *et al.*, Tuning magnetic coupling in Sr_2IrO_4 thin films with epitaxial strain. *Phys. Rev. Lett.* **112**, 147201 (2014).
29. A. Seo *et al.*, Compressive strain induced enhancement of exchange interaction and short-range magnetic order in Sr_2IrO_4 investigated by Raman spectroscopy. *Phys. Rev. B* **100**, 165106 (2019).
30. B. Kim, P. Liu, C. Franchini, Dimensionality-strain phase diagram of strontium iridates. *Phys. Rev. B* **95**, 115111 (2017).
31. H. Wang *et al.*, Giant anisotropic magnetoresistance and nonvolatile memory in canted antiferromagnet Sr_2IrO_4. *Nat. Commun.* **10**, 2280 (2019).
32. A. S. Everhardt *et al.*, Tunable charge to spin conversion in strontium iridate thin films. *Phys. Rev. Mater.* **3**, 51201 (2019).
33. C. Wang *et al.*, Anisotropic magnetoresistance in antiferromagnetic Sr_2IrO_4. *Phys. Rev. X* **4**, 41034 (2014).
34. H. Gretarsson *et al.*, Two-magnon Raman scattering and pseudospin-lattice interactions in Sr_2IrO_4 and $Sr_3Ir_2O_7$. *Phys. Rev. Lett.* **116**, 136401 (2016).
35. J. Porras *et al.*, Pseudospin-lattice coupling in the spin-orbit Mott insulator Sr_2IrO_4. *Phys. Rev. B* **99**, 085125 (2019).
36. S. J. Moon *et al.*, Temperature dependence of the electronic structure of the J_{eff} = 1/2 Mott insulator Sr_2IrO_4 studied by optical spectroscopy. *Phys. Rev. B* **80**, 195110 (2009).
37. Y. Li *et al.*, Strong lattice correlation of non-equilibrium quasiparticles in a pseudospin-1/2 Mott insulator Sr_2IrO_4. *Sci. Rep.* **6**, 19302 (2016).
38. D. Pincini *et al.*, Anisotropic exchange and spin-wave damping in pure and electron-doped Sr_2IrO_4. *Phys. Rev. B* **96**, 075162 (2017).
39. J. Bertinshaw *et al.*, Spin-wave gap collapse in Rh-doped Sr_2IrO_4. *Phys. Rev. B* **101**, 094428 (2020).
40. H. Gretarsson *et al.*, Persistent paramagnons deep in the metallic phase of $Sr_{2-x}La_xIrO_4$. *Phys. Rev. Lett.* **117**, 107001 (2016).
41. J. Kim *et al.*, Large spin-wave energy gap in the bilayer iridate $Sr_3Ir_2O_7$: Evidence for enhanced dipolar interactions near the mott metal-insulator transition. *Phys. Rev. Lett.* **109**, 157402 (2012).
42. J. Kim *et al.*, Excitonic quasiparticles in a spin-orbit Mott insulator. *Nat. Commun.* **5**, 4453 (2014).
43. M. Moretti Sala *et al.*, Orbital occupancies and the putative j_{eff} = 1/2 ground state in Ba_2IrO_4: A combined oxygen K -edge XAS and RIXS study. *Phys. Rev. B* **89**, 121101(R) (2014).
44. M. Moretti Sala *et al.*, Evidence of quantum dimer excitations in $Sr_3Ir_2O_7$. *Phys. Rev. B* **92**, 024405 (2015).
45. T. Hogan *et al.*, Disordered dimer state in electron-doped $Sr_3Ir_2O_7$. *Phys. Rev. B* **94**, 100401 (2016).
46. X. Liu *et al.*, Anisotropic softening of magnetic excitations in lightly electron-doped Sr_2IrO_4. *Phys. Rev. B* **93**, 241102 (2016).
47. X. Lu *et al.*, Doping evolution of magnetic order and magnetic excitations in $(Sr_{1-x}La_x)_3Ir_2O_7$. *Phys. Rev. Lett.* **118**, 027202 (2017).
48. X. Lu *et al.*, Dispersive magnetic and electronic excitations in iridate perovskites probed by oxygen K-edge resonant inelastic x-ray scattering. *Phys. Rev. B* **97**, 041102 (2018).
49. L. J. P. Ament, G. Khaliullin, J. Van Den Brink, Theory of resonant inelastic x-ray scattering in iridium oxide compounds: Probing spin-orbit-entangled ground states and excitations. *Phys. Rev. B* **84**, 020403(R) (2011).
50. C. Bhandari, Z. S. Popović, S. Satpathy, Electronic structure and optical properties of Sr_2IrO_4 under epitaxial strain. *New J. Phys.* **21**, 13036 (2019).
51. O. Ivashko *et al.*, Strain-engineering mott-insulating La_2CuO_4. *Nat. Commun.* **10**, 786 (2019).
52. J. G. Vale *et al.*, Importance of XY anisotropy in Sr_2IrO_4 revealed by magnetic critical scattering experiments. *Phys. Rev. B* **92**, 020406 (2015).
53. R. Coldea *et al.*, Spin waves and electronic interactions in La_2CuO_4. *Phys. Rev. Lett.* **86**, 5377–5380 (2001).
54. H. Watanabe, T. Shirakawa, S. Yunoki, Theoretical study of insulating mechanism in multiorbital Hubbard models with a large spin-orbit coupling: Slater versus Mott scenario in Sr_2IrO_4. *Phys. Rev. B* **89**, 165115 (2014).
55. H. Gretarsson *et al.*, Crystal-field splitting and correlation effect on the electronic structure of A_2IrO_3. *Phys. Rev. Lett.* **110**, 076402 (2013).
56. K. Wang *et al.*, Mott transition and collective charge pinning in electron doped Sr_2IrO_4. *Phys. Rev. B* **98**, 045107 (2018).
57. B. H. Kim, G. Khaliullin, B. I. Min, Electronic excitations in the edge-shared relativistic Mott insulator: Na_2IrO_3. *Phys. Rev. B* **89**, 081109 (2014).
58. E. M. Plotnikova, M. Daghofer, J. van den Brink, K. Wohlfeld, Jahn-Teller effect in systems with strong on-site spin-orbit coupling. *Phys. Rev. Lett.* **116**, 106401 (2016).
59. C. Monney *et al.*, Mapping of electron-hole excitations in the charge-density-wave system 1T-$TiSe_2$ using resonant inelastic x-ray scattering. *Phys. Rev. Lett.* **109**, 047401 (2012).
60. E. M. Pärschke, K. Wohlfeld, K. Foyevtsova, J. van den Brink, Correlation induced electron-hole asymmetry in quasi- two-dimensional iridates. *Nat. Commun.* **8**, 686 (2017).
61. M. Souri *et al.*, Optical signatures of spin-orbit exciton in bandwidth-controlled Sr_2IrO_4 epitaxial films via high-concentration Ca and Ba doping. *Phys. Rev. B* **95**, 235125 (2017).
62. R. M. Ribeiro, V. M. Pereira, N. M. R. Peres, P. R. Briddon, A. H. C. Neto, Strained graphene: Tight-binding and density functional calculations. *New J. Phys.* **11**, 115002 (2009).
63. G. Martnez, P. Horsch, Spin polarons in the t-J model. *Phys. Rev. B Condens. Matter* **44**, 317–331 (1991).
64. V. N. Strocov *et al.*, High-resolution soft X-ray beamline ADRESS at the Swiss Light Source for resonant inelastic X-ray scattering and angle-resolved photoelectron spectroscopies. *J. Synchrotron Radiat.* **17**, 631–643 (2010).
65. M. M. Sala, C. Henriquet, L. Simonelli, R. Verbeni, G. Monaco, High energy-resolution set-up for ir l3 edge rixs experiments. *J. Electron Spectrosc. Relat. Phenom.* **188**, 150–154 (2013).
66. Y. V. Shvyd'ko *et al.*, MERIX-next generation medium energy resolution inelastic x-ray scattering instrument at the aps. *J. Electron Spectrosc. Relat. Phenom.* **188**, 140–149 (2013).
67. E. M. Pärschke, R. Ray, Influence of the multiplet structure on the photoemission spectra of spin-orbit driven Mott insulators: Application to Sr_2IrO_4. *Phys. Rev. B* **98**, 064422 (2018).